AIAA JOURNAL
Vol. 33, No. 1, January 1995

Eulerian/Lagrangian Coupling Procedure for Three-Dimensional Vortical Flows

Hélène M. Felici*
Swiss Federal Institute of Technology, 8092 Zurich, Switzerland
and
Mark Drela†
Massachusetts Institute of Technology, Cambridge, Massachusetts 02139

A coupled Eulerian/Lagrangian method is presented to reduce the numerical diffusion observed in solutions of three-dimensional vortical flows using Eulerian finite volume time-marching schemes. A Lagrangian particle tracking method, added to the Eulerian scheme, provides a correction of the Eulerian solution. In turn, the Eulerian solution is used to integrate the Lagrangian state vector along the particles trajectories. While the Eulerian solution insures the mass conservation and sets the pressure field, the particles describe accurately the convection properties and enhance the vorticity and entropy capturing capabilities of the Eulerian solver. The Eulerian/Lagrangian coupling strategies are discussed and the combined scheme is tested on a constant stagnation pressure flow in a 90-deg bend and on a swirling flow in a pipe. As the numerical diffusion is reduced with the Lagrangian correction, a vorticity gradient augmentation is identified as a problem linked to the inviscid representation. The addition of a Lagrangian pseudodiffusion term to the combined scheme reveals a solution to the problem. The resulting solution still shows much lower diffusion than the basic Eulerian one. The reduction of numerical diffusion is quantified by comparing the combined scheme solutions with finer grid Eulerian results.

Nomenclature

C_p	= pressure coefficient
N	= trilinear function
p	= static pressure
p_0	= stagnation pressure
R	= pipe radius
$\boldsymbol{r}$	= position vector
S	= entropy related function, p/ρ^γ
T_l	= Lagrangian source term
t, t_l	= Eulerian and Lagrangian times
U, U_l	= Eulerian and Lagrangian state vectors
u, v, w	= Cartesian velocity components in x, y, z directions
$\boldsymbol{v}$	= velocity vector
γ	= ratio of specific heats
Γ	= circulation
$\Delta t, \Delta t_l$	= Eulerian and Lagrangian time steps
ϵ_{p0}	= L_2 norm of stagnation pressure losses
ν_l	= Lagrangian pseudodiffusion coefficient
ξ, η, ζ	= cell-centered local coordinate system
ρ	= static density
σ, τ	= local coordinate system on a cell face
Ψ	= stream function
$\boldsymbol{\omega}$	= vorticity vector

Subscript

in	= inlet

Superscript

$n, n+1$	= time indices

Presented as Paper 93-3370 at the AIAA 11th Computational Fluid Dynamics Conference, Orlando, FL, July 6–9, 1993; received July 10, 1993; revision received June 16, 1994; accepted for publication June 20, 1994.

*Research Associate, Institute of Energy Technology. Member AIAA.
†Associate Professor, Department of Aeronautics and Astronautics. Member AIAA.

I. Introduction

THE continuous improvement in CPU and memory capabilities of supercomputers has rendered practical the solution of flow problems of more and more complex nature. However, the efficient numerical treatment of flow nonhomogeneities, such as vortex wakes or tip vortex roll-up, embedded in a smooth background flow, remains a challenging field of study. In many applications, the prediction of the strength and position of these regions is of primary importance. For instance, the flow around a helicopter rotor shows a strong interaction between the shed vortices off one blade and the following blade. The prediction of the resulting loads requires the accurate solution of the shed vortices' trajectories and of the interaction phenomenon. In the case of a bend with a pump located at the bend exit, the location and strength of the secondary flow must be solved accurately, since noise and performance losses may result from the impingement of the secondary vortex on the rotating blades.

These phenomena are characterized by transverse length scales differing by orders of magnitude from the length scale of the supporting flow (the transverse length scale of trailing vortices has been found experimentally to be as low as 5% of the airfoil chord[1]). Since these features often cover a convection length much higher than their intrinsic length, the prediction of vortex-dominated flows is highly sensitive to small local errors. This makes these features difficult to be captured by finite difference methods.

The approaches taken to efficiently resolve small size flow features result from a compromise between computer requirements and solution accuracy. The accuracy of the solution is linked to grid resolution when using an Eulerian or a Navier–Stokes solver, since poor solution representation is a common feature of these solvers in regions of high gradients and small length scales with respect to the background flow. This leads to grid refinement (adaptative, zonal or multigrid solutions[2]), to the use of a priori known solutions and analytical flow models correcting the solution (perturbation methods[3]), or to more accurate discretization/integration algorithms.[4] In potential methods with fitted sheets,[5] not susceptible to numerical diffusion, the a priori knowledge of the vortex structure or position is required, whereas spectral methods do not allow discontinuities in the solution and are difficult to apply on domains of complex shape. Vortex methods such as the one used by Leonard[6] are based on Biot–Savart law and restricted to

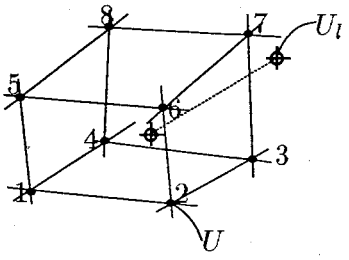

Fig. 1 Eulerian and Lagrangian state vectors defined at nodes and at marker location, respectively.

incompressible flows. The "cloud-in-cell" technique[7] uses stream functions and is restricted to two-dimensional incompressible flows. All of these studies were prompted by the large influence of these small size nonhomogeneities regions on the overall flow solution.

The Euler equations are chosen as the base of the present method because of the inherent capturing of embedded vorticity. The reduction of the numerical diffusion observed in standard Eulerian finite volume time-marching calculations is achieved through the coupling of the Euler and the Lagrange equations. In addition to the Eulerian solution, state vectors and trajectories of Lagrangian particle markers are integrated as these markers convect through the Eulerian grid. The Lagrangian information is used to correct the numerical diffusion of the Eulerian solution.

Incompressible internal cases are presented here, but the method is described for both compressible and incompressible flows. The external flow case of a trailing vortex behind a three-dimensional wing and an unsteady Lamb vortex convection case have been investigated by Felici and Drela[8] and Felici,[9] respectively. Extension to viscous and shock flows is feasible; see the work of Felici[9] and Drela and Murman.[10]

Section II presents the Lagrangian integration technique. The particle markers integration and initial positioning are discussed in Sec. III. In Secs. IV and V, the method is applied to a constant stagnation pressure flow in a bend and to a swirling flow in a pipe. In the latter case, a vorticity gradient augmentation is identified that leads to a destabilization of the method. A solution is proposed as the introduction of a pseudodiffusion in the Helmholtz equation. Conclusions are presented in Sec. VI.

II. Methodology

The method is based on the approach of Drela and Murman[10] for compressible flows in two-dimensions and is extended here to include three-dimensional and incompressible flow cases. The combination of the Eulerian and the Lagrangian solvers takes advantage of both the accurate convection description of the Lagrangian technique and the "elliptic" representation of the Eulerian solution enforcing the mass conservation and setting the pressure field. The Lagrangian solution is based on particle markers carrying vorticity and entropy and convecting with the local flow through the Eulerian grid. The Eulerian solver provides the source terms required for the Lagrangian integration. In turn, the Lagrangian solution, immune to numerical diffusion, accurately captures the convection of vorticity and entropy. This is used to locally correct the Eulerian solution and to reduce its numerical diffusion errors.

The numerical method, described by Felici,[9] is only outlined here. The Euler equations are solved using a node-based Ni-Lax-Wendroff algorithm on an unstructured grid for compressible and incompressible (with the artificial compressibility concept[11]) flows. The numerical smoothing is based on a second difference for compressible flows and on a fourth difference (second-order accurate on distorted grids) for incompressible flows. The far-field conditions use the one-dimensional characteristics theory.

Figure 1 shows the Eulerian state vector defined at the nodes of the cell, with one Lagrangian marker flowing through the cell at the local speed. For the Lagrangian integration, a local cell-centered coordinate system (ξ, η, ζ) is set up in each cell to define eight trilinear functions

$$N_{1,\ldots,8} = \tfrac{1}{8}(\xi \pm 1)(\eta \pm 1)(\zeta \pm 1) \tag{1}$$

used to interpolate any flow value required at a marker location from the Eulerian flow values defined at the nodes of the cell containing the marker. By using a system of neighboring cells, the pointers identifying the location of a marker in a given cell are readily updated when the marker flows through the grid.[9] The local coordinates of a marker in a cell, used to interpolate Eulerian flow values from nodes to marker, are rapidly found by solving an implicit system for ξ, η, ζ,

$$\boldsymbol{r} = \sum_{k=1}^{8} N_k \boldsymbol{r}_k \tag{2}$$

by a few Newton-Raphson iterations. $\boldsymbol{r}$ and $\boldsymbol{r}_k$ are the marker and node locations, respectively. The Lagrangian state vector U_l and source term T_l are related by

$$\frac{\mathrm{D}U_l}{\mathrm{D}t} = T_l \tag{3}$$

with D/Dt being the material derivative and

$$U_l = \begin{bmatrix} \boldsymbol{r} \\ \boldsymbol{\omega} \\ S \end{bmatrix}, \qquad T_l = \begin{bmatrix} \boldsymbol{v} \\ (\boldsymbol{\omega}\cdot\nabla)\boldsymbol{v} - \boldsymbol{\omega}(\nabla\cdot\boldsymbol{v}) - \nabla\left(\frac{1}{\rho}\right)\times\nabla p \\ 0 \end{bmatrix} \tag{4}$$

for a compressible flow. For a constant density flow

$$U_l = \begin{bmatrix} \boldsymbol{r} \\ \boldsymbol{\omega} \end{bmatrix}, \qquad T_l = \begin{bmatrix} \boldsymbol{v} \\ (\boldsymbol{\omega}\cdot\nabla)\boldsymbol{v} \end{bmatrix} \tag{5}$$

The vorticity is represented by $\boldsymbol{\omega} = \nabla \times \boldsymbol{v}$.

For steady-state cases, the markers can convect at any speed, and the Eulerian and Lagrangian solutions do not need to be time integrated using the same time steps during the time-marching convergence. In unsteady flows, the time steps have to be identical, since at each instant the markers represent the current state vector of a particle. The time integration of U_l is performed using a predictor-corrector scheme

$$U_l(t_l + \Delta t_l) = U_l(t_l) + 0.5\Delta t_l\left([T_l]_r^n + [T_l]_{r_p}^{n+1}\right) \tag{6}$$

where the values within brackets are determined at the old marker location $\boldsymbol{r}$ by using the Eulerian flow at time t (and the interpolating function N) for the predictor step and at the predicted marker location $\boldsymbol{r}_p$ by using the Eulerian flow at time $t + \Delta t$. Depending on the Eulerian/Lagrangian coupling sequence, predicted and corrected values both can also be based on the Eulerian solution at time t, as shown later. The spatial derivatives required at the marker location are a byproduct of the solution of Eq. (2); see Felici.[9]

The coupling sequence is then completed by a "correction step" where the markers are used to reduce the numerical diffusion of the Eulerian solution. First, a vorticity correction is performed where the vorticity attached to a marker is used to alter the velocity components at the cell nodes. Then, an entropy correction takes place for the compressible flow cases. The two correction procedures are described by Felici and Drela.[12] Briefly, by comparing Eulerian and Lagrangian values of entropy and vorticity at the marker location, an error is defined and distributed back to the nodes in the case of the entropy correction and to the cell centers in the case of the vorticity correction.

When an entropy correction is found at a node, it is translated into changes in density and energy in the Eulerian state vector (assuming no change in p, ρu, ρv, and ρw). Another option is to keep p, u, v, and w constant, thus insuring no change in vorticity while correcting the density, mass, and energy in the Eulerian solution (since the vorticity correction is a separate procedure). Both formulations gave similar results on a Lamb vortex convection.[9]

For the vorticity correction, a solid-body rotation was previously used[12] to get velocity changes at the grid nodes from the vorticity error at a cell center. Here, the method of Drela and Murman[10] has been extended to three dimensions where the vorticity error $\Delta\boldsymbol{\omega}$ at

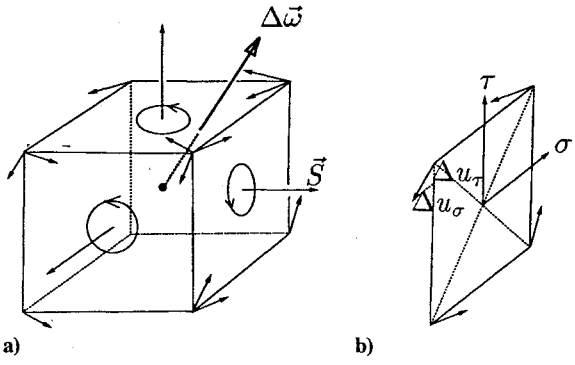

Fig. 2 a) Error in circulation $\Delta\Gamma$ on each face from error in vorticity $\Delta\vec{\omega}$ at cell center, and b) corrections in coordinate system local to the face.

the cell center gives a circulation error $\Delta\Gamma$ around each cell face, as shown in Fig. 2, by

$$\Delta\Gamma = \Delta\omega \cdot S \tag{7}$$

where S is the face surface vector. On each face, $\Delta\Gamma$ serves to find velocity corrections at the four corner nodes in a coordinate system (σ, τ) local to the face (see Fig. 2b),

$$\Delta\Gamma = \int \Delta u_\sigma \, d\sigma + \Delta u_\tau \, d\tau \tag{8}$$

If the magnitude of the eight components of velocity corrections is set identical, Eq. (8) gives the velocity corrections at the four face nodes. As opposed to the solid-body distribution, this gives identical corrections for faces of same area/perimeter ratio, independently of the face length/width ratio. The contributions from each face are then added at a node to get the final velocity correction. The correct circulation around each face is obtained by iteratively recomputing $\Delta\Gamma$, the velocity corrections, and their sum at a node. The convergence rate of this recursive procedure is second-order.[9]

Each marker influences the Eulerian solution only locally, which makes this scheme well suited for three-dimensional flow solutions (CPU reduction). Also, the Lagrangian solution is needed only in regions of interest as markers can be located selectively in the flow. No a priori information is required on the flow structure when markers are integrated downstream since the Lagrangian solution includes inherently "convective" capabilities. The feasibility, efficiency, and flexibility of this method has been demonstrated by Felici[9] by application to different flow problems (i.e., three-dimensional steady, unsteady, internal, external as well as compressible and incompressible inviscid flow cases).

Next, the comparative advantages of two strategies of trajectory integration and/or marker positioning are described for representative flow situations.

III. Markers Integration/Distribution

A. Downstream Integration

The more straightforward option is to position the markers at the inlet of the domain and to trace them as they convect downstream with the local Eulerian flow. At each time step along their trajectories, the Lagrangian state vectors are obtained by integration of the source terms, and the markers are used to locally correct the Eulerian flow. The initial values for the Lagrangian state vectors are found by interpolating the Eulerian flow in the inlet region, where the Eulerian solution does not significantly suffer from numerical diffusion due to the proximity of the boundary conditions.

Figure 3b shows a vortex convecting (perpendicular to its axis) through a contraction. In this unsteady case, the markers are initially positioned near the vortex core and convect downstream with the vortex. The time step Δt_l used for the trajectories integration must thus be identical to the Eulerian Δt. Figure 3a shows the interaction between Eulerian and Lagrangian schemes: the Eulerian solutions at times t and $t + \Delta t$ (separated by a step of the Lax-Wendroff algorithm: LW) are used to compute the new marker position by

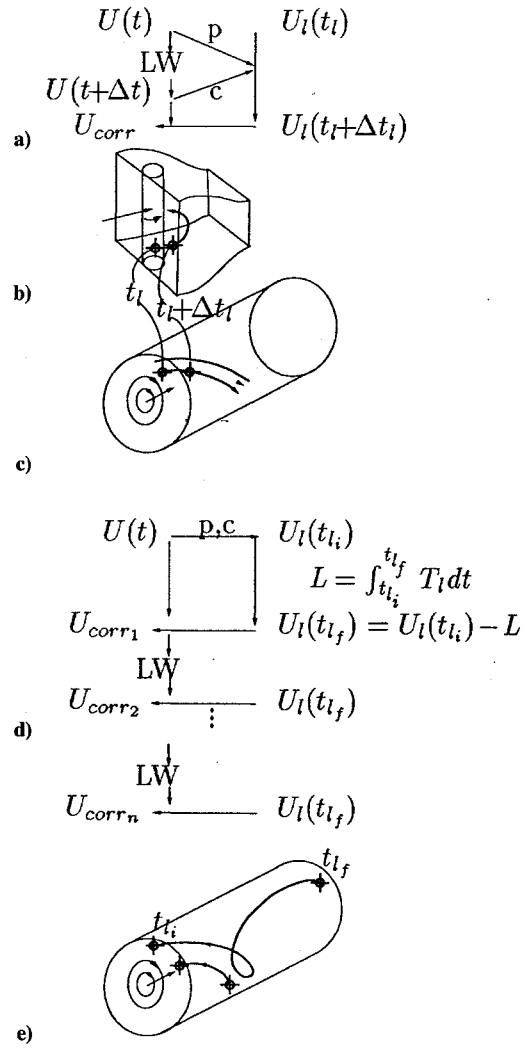

Fig. 3 Eulerian/Lagrangian interaction procedures for *downstream integration* of trajectories: a) schematic of Eulerian/Lagrangian interaction, b) unsteady vortex convection in contraction, and c) steady swirling flow in pipe; for *upstream integration* of trajectories, d) schematic of Eulerian/Lagrangian interaction, and e) steady swirling flow in pipe.

the predictor-corrector scheme (p,c) of Eq. (6). The new values of vorticity and entropy are also computed using Eq. (6). The new Lagrangian state vector is then used to correct the Eulerian state vector for each cell containing a marker at time $t + \Delta t$.

Figure 3c shows a steady swirling flow in a pipe. Here, the markers are injected at the inlet of the domain at regular time intervals with approximately one marker per cell in the vortical regions. As the markers convect downstream and exit the domain, new ones are injected. The Eulerian and Lagrangian time steps do not need to be equal, and Δt_l is fixed by the accuracy of the trajectory integration. The two solvers interaction is described by Fig. 3a.

In a downstream integration, no a priori knowledge of the location or structure of the flow features is necessary. For an unsteady flow, the markers are initially positioned in the feature area and the use of identical Lagrangian and Eulerian time steps implies the presence of markers in the feature area at each time. For the steady swirling flow, the markers can be positioned in the entire inlet section. However, it can be seen that placing markers only near the pipe wall at the inlet suffice to trace the vorticity downstream.

In this case, however, the convecting markers are subjected to a strong redistribution, so that an even correction of the Eulerian flow is not obtained where needed. To get an even distribution of markers in the areas to correct, a coupling strategy called "upstream integration" is used.

B. Upstream Integration

This second interaction strategy is illustrated in Figs. 3d and 3e. For the steady swirling flow, the markers are initially placed at each

cell center in the whole domain, and the trajectories and source terms are integrated upstream [with a predictor-corrector algorithm (p,c) on the Eulerian field at time t] until the inlet is reached; see Fig. 3d. The Lagrangian time step is again fixed by accuracy of the trajectory integration. At the inlet, the Lagrangian state vector $U_l(t_{l_i})$ is found by interpolating the local Eulerian solution to the markers location. By subtracting the integrated source terms L from the inlet state vector, the Lagrangian state vector at each cell center is found. Then the correction procedure takes place evenly from each cell center, and the Lax-Wendroff algorithm (LW) is applied on the corrected solution. The trajectories could now be recomputed, but it has been found that iterating the correction step and the LW step, while keeping the Lagrangian state vectors and the trajectories fixed, leads to a faster convergence. However, to insure stability, the trajectories should be recomputed before the Eulerian solution changes are too large. Also, the trajectories do not have to be traced till the inlet but can be stopped at any previous upstream location. If the trajectories are stopped before, the corrections are smaller, and the convergence is slower, since the full correction is obtained only when the cells where the markers stop have themselves been fully corrected. Again, to minimize CPU time, the markers can be placed only in the regions where corrections are required.

For unsteady flows with an upstream integration, the trajectories have to be recomputed at each Eulerian time. The trajectories can be integrated until the inlet is reached or over only a few time steps. At any position, though, the Eulerian solution at that particular time is required to compute the source terms and the trajectories. Thus, to minimize the number of Eulerian solutions to store, the trajectories can be integrated backwards over one time step only. This remains, however, a cumbersome procedure.

Thus, for unsteady flows, the downstream integration is simpler and more efficient. For steady flows, the upstream integration allows a spatially even correction process. This was more successful in swirling flow cases where strong redistributions occur. Next, the trajectory integration is discussed in relation with the positioning of the markers.

C. Positioning of the Markers

The fact that markers are needed only where a correction is required becomes particularly useful (CPU-wise) for features concentrated in a smooth background flow.

In a downstream integration, the built-in convection properties of the Lagrangian technique allow for the steady or unsteady tracing of features without an a priori knowledge of their position or structure. In an upstream integration, the area covered by the flow features must be broadly known. It is usually possible to determine the areas to correct from a basic knowledge of the flow. However, in cases like the secondary flow in a pipe, the features are so dispersed that the markers have to fill the whole flow.

In a downstream convection, the weighting functions of Eq. (1) serve to distribute corrections to the nodes since at any time the markers are not distributed uniformly in the Eulerian grid. Moreover, the divergence/convergence of the trajectories can create holes in the markers distribution (see Fig. 4a). In the field, some nodes are not influenced by any marker, whereas others are influenced by several markers. With large corrections of the Eulerian solution, this nonuniformity can lead to numerical instability.

In the upstream integration, weighting functions are not used since the corrections occur uniformly from the cell centers and the problem of redistribution of the markers does not occur (see Fig. 4b). Nevertheless, the upstream integration is less suitable for unsteady flow calculations.

The Lagrangian state vector is taken as piecewise constant in a cell, so that the representation of strong gradients is inaccurate on coarse grids. In Fig. 4c, using the weighting factors in a downstream integration results in an average correction for the field cells, an inaccurate procedure for flows with high gradients. For the upstream integration shown in Fig. 4d, the presence of one marker per cell is insured. However, because of the lack of grid resolution, when the markers trajectories are diverging upstream, the distribution of markers is sparse in the inlet region. The inlet information between the two streamlines is not "seen" or transported by the markers.

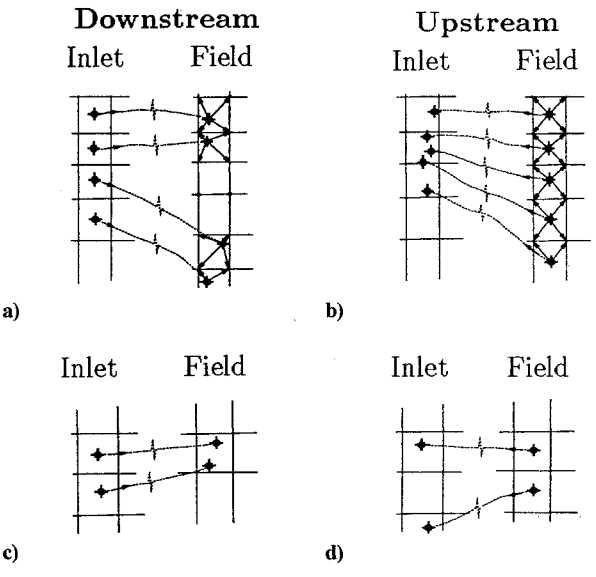

Fig. 4 Markers redistribution during downstream or upstream trajectories integration leads to a) lack of correction of the Eulerian solution, b) even correction, c) average in cell, and d) sparse distribution of markers in the inlet region leading to inaccurate representation of inlet flow values by the Lagrangian markers.

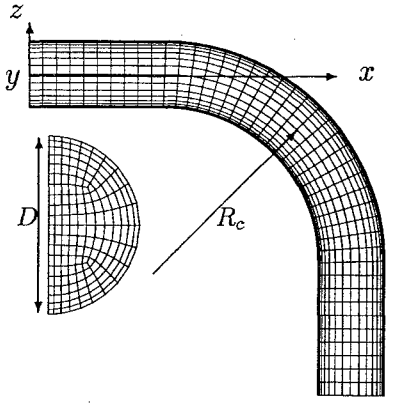

Fig. 5 Coarse grid front and side views (189 × 43 nodes), D = 0.048 m, R_c/D = 2.8.

Figures 4c and 4d illustrate a problem linked to a lack of grid resolution. As will be shown later, the gradients are weaker in an Eulerian solution because of numerical diffusion. The Lagrangian solution, however, being immune to numerical diffusion, allows us to represent stronger gradients.

Thus, the lack of grid resolution can lead to problems with upstream or downstream integrations. In Sec. V, this issue is further addressed with a swirling flow case.

IV. Constant Stagnation Pressure Flow

The incompressible flow in a 90-deg bend of circular cross section is used as a test case to assess the capability of the proposed method. By setting constant inlet velocity and inlet pressure conditions, a flow at constant stagnation pressure p_0 should be computed in the bend since p_0 remains constant along a streamline and each streamline carries the same p_0 value in this case. Also, the field vorticity should be zero since the flow is irrotational upstream of the inlet section.[13] Alternatively, the growth of streamwise vorticity being only a function of the stagnation pressure field, no streamwise vorticity should be created.[14] The exact solution for this flow is then very simple and allows direct comparison with Eulerian as well as Eulerian/Lagrangian results.

By symmetry, the computations are performed on one-half of the pipe, and the bend geometry is taken from the data set of Enayet et al.[15] The computational domain extends two diameters upstream and downstream of the bend inlet and exit sections. The coarse grid

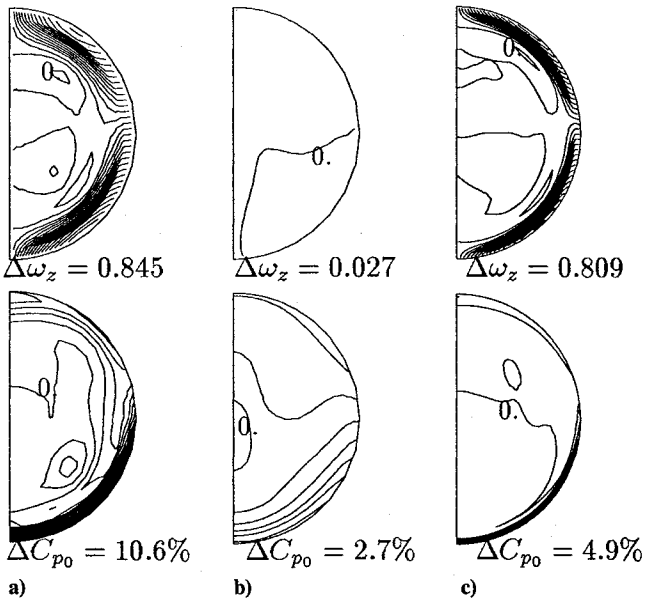

Fig. 6 Top: contours of normalized streamwise vorticity (inc. = 5%) at bend exit cross section, bottom: contours of local error in stagnation pressure coefficient ΔC_{p0} (inc. = 0.5%); a) Eulerian solution, b) Eulerian/Lagrangian solution, and c) Eulerian solution on fine grid.

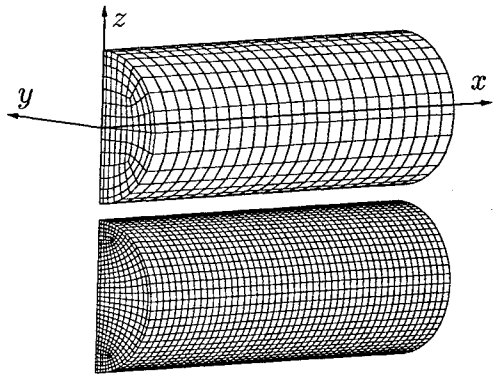

Fig. 7 Straight circular pipe computational grids: coarse grid with 125 × 25 nodes and fine grid with 384 × 49 nodes (radius/length = 5.52).

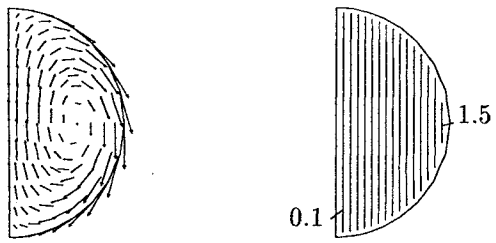

Fig. 8 (C = 0.2) Crossflow velocity vectors and axial vorticity on inlet cross section (coarse grid).

shown in Fig. 5 is composed of 43 × 189 nodes. The fine grid is composed of eight times as many cells as the coarse grid. Note the mixing of the H and O mesh topologies to form an unstructured grid in the cross planes. This avoids singularities at both walls and centerline. Eulerian solutions are computed on both grids, whereas an Eulerian/Lagrangian solution is computed on the coarse grid only. The Lagrangian procedure uses an upstream streamline integration, and the streamlines are integrated backwards with approximately two steps per cell until the inlet is reached. The streamlines are recomputed every 50 Eulerian iterations and an under-relaxation on the vorticity correction is used to limit the perturbations to the Eulerian solver (under-relaxation factor of 0.5%).

Contours of streamwise vorticity (z component) are shown in Fig. 6 (top) for the bend exit cross section for the coarse and fine grid Eulerian solutions and for the coarse grid Eulerian/Lagrangian solution. The maximum error in vorticity (normalized by the ratio of inlet velocity to pipe radius U_{in}/R) is indicated. The combined scheme is very effective at reducing the vorticity errors, whereas the Eulerian solution on a finer mesh shows much less reduction. The local error in stagnation pressure coefficient is defined at a node by $\Delta C_{p0} = 2(p_{0_{in}} - p_0)/(\rho U_{in}^2)$ and is shown in Fig. 6 (bottom). This error in the combined solution is reduced locally when compared with the coarse grid Eulerian solution. The maximum error in ΔC_{p0} for the Eulerian/Lagrangian solution is even lower than for the fine grid Eulerian solution. Since the stagnation pressure is not transported along the streamlines in the Lagrangian scheme, the correction of the stagnation pressure occurs indirectly through the vorticity correction (Crocco's equation relates vorticity and stagnation pressure gradient). The corrected velocities alter the Lax-Wendroff cell flux balance so that the pressure is corrected too.

A global indicator of losses is the L_2 norm of the stagnation pressure losses defined as an average over the N nodes by

$$\epsilon_{p0} = \sqrt{\sum_{i=1}^{N} (\Delta C_{p0_i})^2 / N}$$

Even if the maximum local error in stagnation pressure is smaller in the Eulerian/Lagrangian solution than in the fine grid Eulerian solution, the errors are less diffused in the latter, so that a node-averaged measure like the L_2 norm gives a less favorable result for the Eulerian/Lagrangian solution. The L_2 norm of the stagnation pressure errors decreases by a factor of ~2.3 with the Eulerian/Lagrangian solution, whereas the Eulerian solution on the finer grid leads to a reduction factor of ~4.0 (in accordance with the second-order accuracy of the Lax-Wendroff scheme).

The addition of the Lagrangian correction leads to a computer time increase of ~75% over the coarse grid Eulerian solution. In comparison, the fine grid Eulerian solution requires 16 times more computer time than the coarse grid Eulerian solution.

V. Swirling Flow

The computation of an incompressible swirling flow in a straight circular pipe with an inlet crossflow modeled as two counter-rotating vortices is presented. By symmetry, a half-pipe geometry is used. The calculations are performed on a coarse and a fine grid shown in Fig. 7 with 25 × 125 nodes and 49 × 384 nodes, respectively. The inlet crossflow is found from the Poisson equation $\nabla^2\Psi = -\omega_x$, with $\Psi = -Cy[1 - (y^2 + z^2)/R^2]$, relating the streamfunction Ψ to the axial vorticity ω_x. The term C measures the strength of the swirling flow. With a chosen maximum inlet crossflow velocity of 40% of the uniform convection velocity (C = 0.2), the inlet crossflow and axial vorticity are shown in Fig. 8 on the coarse grid.

The Eulerian and Eulerian/Lagrangian calculations are performed on both grids. In the combined scheme, the markers are positioned at each cell center, and the streamlines are integrated upstream with approximately two steps per cell. The streamlines are recomputed every 50 Eulerian iterations. To limit the perturbations to the Eulerian solver, the corrections are multiplied by a factor of $\frac{1}{4}$.

The circulation Γ around a closed curve serves to quantify the numerical diffusion. In a barotropic flow subjected to a conservative force field with negligible viscous effects, Kelvin's theorem states that the circulation around an arbitrary closed curve moving with the fluid remains constant,

$$\frac{D\Gamma}{D}t = 0 \tag{9}$$

where $\Gamma = \oint v \cdot dr$. The convection of a material curve is obtained by setting "convective" markers in a closed-curve pattern in the flow in the steady-state solution. These markers are traced similarly to the "corrective" markers, upstream or downstream. The curve, placed around the pipe inlet, convects downstream. Figure 9 shows the initial and final curve locations and Γ as a function of the curve convection distance. The coarse grid Eulerian solution exhibits the

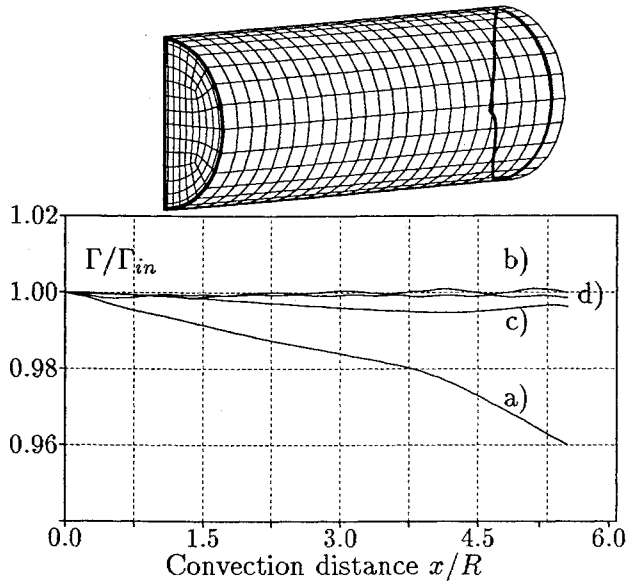

Fig. 9 (C = 0.2) Top: Initial and final circulation contours, bottom: circulation on a closed curve as a function of the distance along the pipe: a) coarse grid Eulerian solution, b) coarse grid Eulerian/Langrangian solution, c) fine grid Eulerian solution, and d) fine grid Eulerian/Langrangian solution.

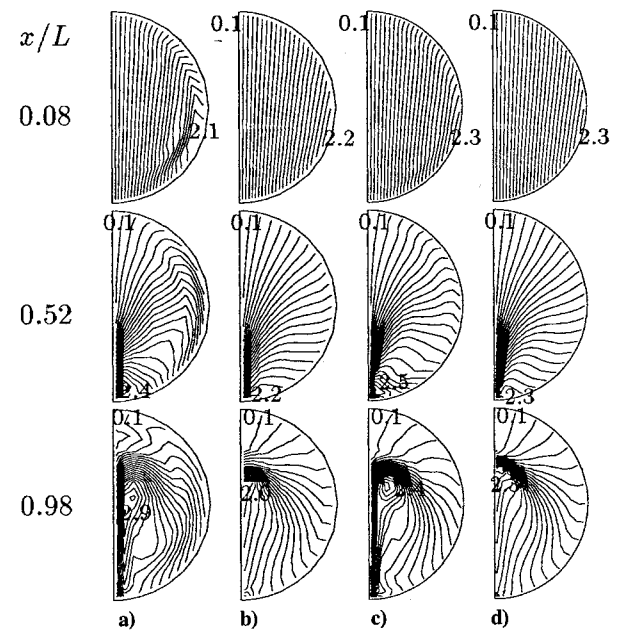

Fig. 10 (C = 0.3) Axial vorticity contours at three cross sections along pipe: a) coarse grid Eulerian solution, b) coarse grid Eulerian/Langrangian solution, c) fine grid Eulerian solution, and d) fine grid Eulerian/Langrangian solution.

largest change in Γ. With the combined scheme on the coarse grid, the change in Γ is reduced by a factor of ~4 near the pipe exit. The circulations for the fine grid Eulerian and Eulerian/Lagrangian solutions are comparable since the correction is much smaller than in the coarse grid cases.

Figure 10 presents the axial vorticity contours on three pipe cross sections for $C = 0.3$ and for the Eulerian and Eulerian/Lagrangian solutions on the coarse and fine grids. Along the pipe, the contours undergo a rotation, and the condition of zero axial vorticity at the symmetry surface leads to a concentration of axial vorticity contours. At the third station, the numerical diffusion near the symmetry surface spreads the vorticity gradient on several cells in the Eulerian solutions. In the combined scheme solutions, the vorticity gradient concentrated on one cell at the symmetry does not show in the plots since the vorticity contours are drawn between cell centers. Comparing coarse grid Eulerian and Eulerian/Lagrangian solutions, the effect of the numerical diffusion is seen in the Eulerian solution as a curving of the axial vorticity contours near the pipe wall (inducing smaller velocities and circulation around the pipe). The fine grid Eulerian solution still shows numerical diffusion near the pipe wall but is in good agreement with the coarse grid Eulerian/Lagrangian solution. Finally, the good agreement of coarse and fine grid Eulerian/Lagrangian solutions shows the efficiency of the scheme on coarse grids already.

In the coarse grid case, the computer time increase due to the introduction of the Lagrangian correction is ~33% of the basic Eulerian solution. In comparison, the fine grid Eulerian solution requires 16 times more computer time than the coarse grid Eulerian calculation (starting from a uniform flow).

In Fig. 10, a strong vorticity gradient region is created corresponding to a vorticity gradient augmentation phenomenon. The fine grid solutions exhibit the same behavior, but in the Eulerian/Lagrangian solution, the vorticity gradient is more intense and spread over one cell only. As the strength of the inlet swirl is increased, the width of this vorticity gradient region decreases. The vorticity field becomes poorly represented (either on the Eulerian grid or by markers located at cell centers in the Lagrangian scheme). This poor sampling rate of the vorticity field leads to inaccurate corrections of the Eulerian solution and affects adversely the convergence of the Eulerian/Lagrangian scheme. In the next section, the strain and vorticity fields are identified as the sources for the vorticity gradient augmentation and a solution is proposed as the introduction of a pseudodiffusion in the Helmholtz equation.

A. Vorticity Gradient Augmentation

The evolution of the scalar field in a flow with high vorticity concentration has been previously studied by Knio and Ghoniem.[16] As the strength of the inlet swirl is increased, the gradients of vorticity, shown in Fig. 10, intensify near the pipe exit. This phenomenon of vorticity gradient augmentation is also intensified when the Lagrangian correction is applied because of the reduction of numerical diffusion.

In Fig. 11, the convergence of three streamlines from inlet to exit is shown for the coarse grid Eulerian and Eulerian/Lagrangian solutions for $C = 0.3$. The streamlines end up in the strong vorticity gradient region at the pipe exit. Since the source terms for the vorticity are small (as shown later), the vorticity carried by the markers is essentially equal to the inlet vorticity at the inlet location of the markers. Since this inlet vorticity differs largely between the three markers (see Figs. 11 and 8), a strong vorticity gradient is created when the streamlines merge along the pipe. In the Eulerian solution, the vorticity is not constant along the streamlines due to numerical diffusion, and the creation of a strong vorticity gradient is inhibited. With the Lagrangian correction, the diffusion is reduced, and the solution shows stronger vorticity gradients. These are also accentuated by the stronger swirl and the stronger convergence of the three streamlines in the combined solution.

The creation of the vorticity gradient is explained from the action of the strain and vorticity fields by using the Helmholtz equation for the convective change in vorticity in an incompressible flow

$$D\omega/Dt = (\omega \cdot \nabla)v \tag{10}$$

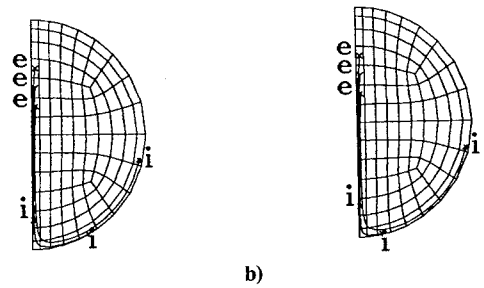

Fig. 11 (C = 0.3) Front view of three streamlines drawn from inlet to exit of the pipe: a) Eulerian solution, and b) Eulerian/Lagrangian solution (i = inlet, e = exit).

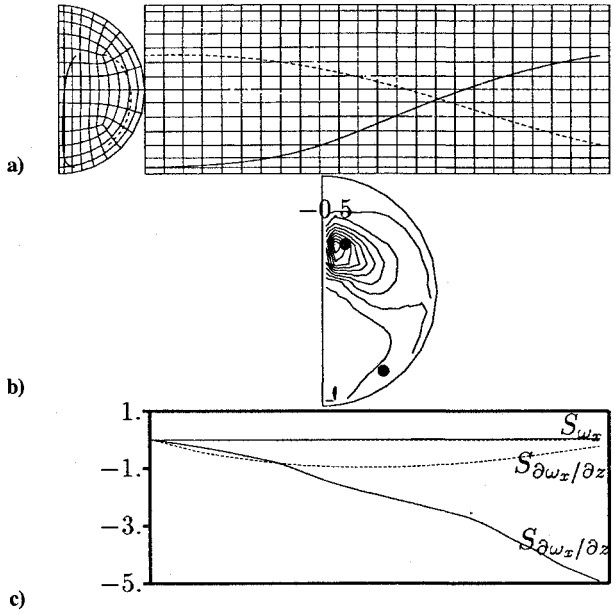

Fig. 12 (C = 0.3): a) two streamlines in front and side views, b) $\partial\omega_x/\partial z$ on exit section with end points of streamlines (inc. = 0.5), and c) source term for axial vorticity: S_{ω_x} and source term for $\partial\omega_x/\partial z$: $S_{\partial\omega_x/\partial z}$ along streamlines.

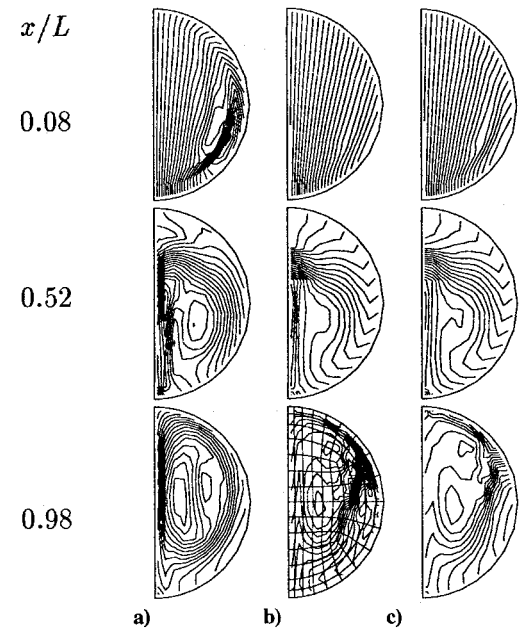

Fig. 13 (C = 0.6) Axial vorticity contours at three cross-sections along the pipe: a) Eulerian solution, b) Eulerian/Lagrangian solution, and c) Eulerian/Lagrangian solution with Helmholtz smoothing term (inc. = 0.2).

The vorticity attached to a particle is governed by the generation of tilting and stretching source terms along the trajectory. With small right-hand side terms, the vorticity will approximately behave as a nondiffusive quantity and

$$\mathrm{D}\omega/\mathrm{D}t \simeq \mathbf{0} \tag{11}$$

The gradient of Eq. (11) gives the behavior of the vorticity gradient for a convecting particle in a steady flow

$$\frac{\mathrm{D}(\nabla\omega_x)}{\mathrm{D}t} = -(\nabla\omega_x \cdot \nabla)\boldsymbol{v} - \nabla\omega_x \times \boldsymbol{\omega} \tag{12}$$

$$\frac{\mathrm{D}(\nabla\omega_y)}{\mathrm{D}t} = -(\nabla\omega_y \cdot \nabla)\boldsymbol{v} - \nabla\omega_y \times \boldsymbol{\omega} \tag{13}$$

$$\frac{\mathrm{D}(\nabla\omega_z)}{\mathrm{D}t} = -(\nabla\omega_z \cdot \nabla)\boldsymbol{v} - \nabla\omega_z \times \boldsymbol{\omega} \tag{14}$$

Thus, if a scalar quantity (here a vorticity component) is constant along a streamline, its gradient is governed along a streamline by the strain and vorticity fields $\nabla\boldsymbol{v}$ and $\boldsymbol{\omega}$.

The main component of vorticity is here in the axial direction x. The behavior of the axial vorticity and of its gradient along a streamline can be written as a function of convection time t from Eqs. (10) and (12) as

$$\omega_x(t) - \omega_x(0) = \int_0^t [(\boldsymbol{\omega} \cdot \nabla)u]\,\mathrm{d}t = S_{\omega_x} \tag{15}$$

$$\nabla\omega_x(t) - \nabla\omega_x(0) = \int_0^t [-(\nabla\omega_x \cdot \nabla)\boldsymbol{v} - \nabla\omega_x \times \boldsymbol{\omega}]\,\mathrm{d}t = S_{\nabla\omega_x} \tag{16}$$

Next, the right-hand sides of Eq. (15) and of the z component of Eq. (16) are integrated along two streamlines. Equation (16) is verified by comparing the increase in the z derivative of the vorticity at the exit of the pipe [given by Eq. (16)] to the vorticity gradient computed directly from the solution at the pipe exit.

In Fig. 12a, two streamlines are shown in front and side views of the pipe. The axial vorticity z derivative $\partial\omega_x/\partial z$ computed directly from the Eulerian/Lagrangian solution at the pipe exit cross section is plotted with the location of the endpoints of the two streamlines in Fig. 12b. Figure 12c shows the right-hand sides of Eq. (15) (S_{ω_x}) and of the z component of Eq. (16) ($S_{\partial\omega_x/\partial z}$) along the two streamlines. The source terms for ω_x are indeed small for both streamlines compared with the axial vorticity magnitude, verifying Eq. (11). The magnitude of the source term for $\partial\omega_x/\partial z$ is larger for both streamlines, and at the pipe exit, it corresponds indeed to the values of vorticity derivative displayed on the pipe exit cross section in Fig. 12b at the indicated endpoint location of the two streamlines. Thus, Eq. (16) is verified for the particular case of these streamlines, and the strain and rotation fields on the equation right-hand side are indeed the mechanism by which large vorticity gradients are created. Also, these vorticity gradients appear in the absence of strong source terms for the vorticity since the vorticity is essentially passively convected.

B. Introduction of a Pseudodiffusion

Because of the grid coarseness, the information at the inlet between two markers is lost (Fig. 11). To transport information from one marker per cell at the inlet, the grid resolution in the crossflow plane would have to be increased by a factor of ~4 near the pipe exit. As the strength of the swirling flow increases, so does the required grid resolution. Also, because of the inviscid representation of the flow, the increase in grid resolution is linked to an increase of vorticity gradient as seen in Fig. 10. Hence, a grid resolution increase is not a solution to the problem.

As the strength of the inlet swirl is increased to C=0.6, the vorticity gradients are further intensified to a point where the gradient region covers less than one cell as shown in Fig. 13. With an Eulerian scheme, the numerical diffusion spreads the gradient over a few cells. With the Lagrangian correction, wiggles appear in the high-vorticity-gradient region because the representation of this region by markers placed at cell centers (or by Eulerian state vectors at the grid nodes) becomes inadequate (as seen when superimposing the grid on the exit cross section in Fig. 13b). This insufficient representation of the flow destabilizes the Eulerian solution through the correction procedure.

As larger size grids do not solve the problem, the gradients have to be "controlled" so as to be supported on the grid. Thus, the Lagrangian correction technique can still be used to reduce numerical diffusion on a fixed grid if a control of the vorticity gradients is achieved. The introduction of a pseudodiffusion term in the Helmholtz equation permits the control of the vorticity gradients as shown next. If the diffusion introduced by this term is maintained lower than the numerical diffusion of the Eulerian scheme, the resulting solution will still show a substantial improvement over the

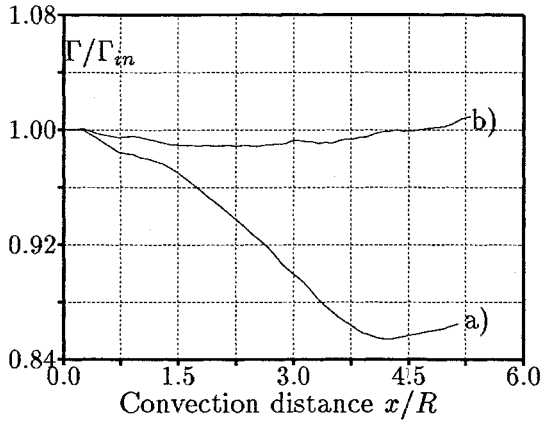

Fig. 14 (C = 0.6) Circulation around a closed curve: a) Eulerian solution, and b) Eulerian/Lagrangian solution with Helmholtz smoothing term.

Eulerian solution alone. The pseudodiffusion term takes a similar form as the real diffusion term arising in a viscous fluid, hence

$$\frac{D\omega}{Dt} = (\omega \cdot \nabla)v + \nu_l \nabla^2 \omega \tag{17}$$

where the coefficient ν_l is proportional to the mesh size h.

A predictor-corrector scheme is used to integrate the pseudodiffusion term along the trajectory. The term is found similarly to the smoothing term in the Lax-Wendroff algorithm, but with ω being known at the cell centers instead of the state vector being known at the nodes for the smoothing. To compute a Laplacian of the vorticity, node values are defined by averaging the values of ω at the eight surrounding cell centers. The Laplacian at a marker location is evaluated by summing the differences between the eight nodes values and the cell center value and interpolating from the cell centers to the marker location at each time. For a wall node, the vorticity gradient at the nearest node to the wall is found by a surface integral of the vorticity over a pseudocell based on cell centers and is extrapolated from this node to the wall node.[9]

Figure 13c shows the axial vorticity for the Eulerian/Lagrangian solution with the addition of a pseudodiffusion term. Because of the control of the vorticity gradients, the vorticity field is more accurately represented on the grid and the combined scheme is stable. The Lagrangian pseudodiffusion is effective at smoothing out the strong vorticity gradients without affecting the smooth vorticity regions. A value of ν_l of 5% was used here.

The diffusion reintroduced in the solution is quantified by measuring the changes in circulation around a closed curve placed around the inlet and moving with the flow. Figure 14 shows the circulation as a function of the average convection distance of the curve for the Eulerian solution and the Eulerian/Lagrangian solution with the addition of the Lagrangian pseudodiffusion. The change in circulation with the latter still remains much smaller than the one observed in the basic Eulerian solution.

VI. Conclusions

The coupling of Eulerian and Lagrangian solution procedures, enabling a correction of the Eulerian state vector based on Lagrangian values and aimed at reducing numerical diffusion errors, has been presented. The addition of built-in convection properties to a standard Eulerian solver resulted in reduced grid density requirements for a given level of accuracy and a better understanding of the true inviscid behavior of the flow, otherwise affected by numerical diffusion. By applying the Eulerian/Lagrangian technique (using point markers flowing at the local speed through the Eulerian grid) to different flow cases, we have shown the need for distinct marker initial locations and trajectory integrations (upstream and downstream). The feasibility and efficiency of the method have been demonstrated by application to a constant stagnation pressure flow in a 90-deg bend and a swirling flow in a pipe.

By increasing the solution accuracy on a given grid, the Eulerian/Lagrangian scheme leads to a more accurate solution of the flow gradients. A vorticity gradient augmentation phenomenon has been identified for the case of a swirling flow in a pipe, resulting in poor vorticity representation on the Eulerian grid and destabilization of the Eulerian/Lagrangian scheme. This is particularly acute in inviscid flow computations where no viscous diffusion occurs to spread the gradients on several grid cells. A solution to this problem has been devised as the addition of a Lagrangian pseudosmoothing in the Helmholtz equation to control the vorticity gradients, without substantially compromising the reduction of numerical diffusion.

The Lagrangian procedure consists of a set of subroutines that can be added a posteriori not only to the present Lax-Wendroff algorithm but to any Eulerian time-marching finite volume algorithm. The flexibility by which corrections to the Eulerian solution can be performed in only chosen areas of the computational domain and the fact that the markers have only a local effect in the cell where they are located help reduce the computer time required by the addition of the Lagrangian scheme. This makes the Eulerian/Lagrangian solver more efficient in flows where nonhomogeneities are more concentrated, and less suited when the vorticity and entropy corrections cover the entire domain. Also, the combined scheme presents built-in convection properties so that an a priori knowledge of the position or strength of the flow nonhomogeneities is not required in a downstream integration of the markers.

Although the results shown here concerned incompressible steady flows, the method is general and has also been applied to unsteady, compressible or external flow cases.[9]

Acknowledgments

This research was sponsored by NASA Ames Research Center with Paul Stremel as technical monitor, by the Office of Naval Research with James A. Fein as technical monitor, and by the National Science Foundation Presidential Young Investigator Program.

References

[1]Roberts, T. W., and Murman, E. M., "Euler Solutions for the Flow Around a Hovering Helicopter Rotor," AIAA Paper 86-1784, June 1986.

[2]Löhner, R., "An Adaptative Finite Element Scheme for Transient Problems in CFD," *Computer Methods in Applied Mechanics and Engineering*, Vol. 61, 1987, pp. 323–338.

[3]Roberts, T. W., "Euler Equation Computations for the Flow over a Hovering Helicopter Rotor," Ph.D. Thesis, Dept. of Aeronautics & Astronautics, Massachusetts Inst. of Technology, Cambridge, MA, Nov. 1986.

[4]Rai, M. M., "Navier-Stokes Simulations of Blade-Vortex Interaction Using High-Order Accurate Upwind Schemes," AIAA Paper 87-0543, Jan. 1987.

[5]Steinhoff, J., and Ramachandran, K., "Free Wake Analysis of Compressible Rotor Flows," AIAA Paper 87-0542, Jan. 1987.

[6]Leonard, A., "Computing Three-Dimensional Incompressible Flows with Vortex Elements," *Annual Review of Fluid Mechanics*, Vol. 17, 1985, pp. 523–559.

[7]Baker, G. R., "The Cloud-in-Cell Technique Applied to the Roll Up of Vortex Sheets," *Journal of Computational Physics*, Vol. 31, 1979, pp. 76–95.

[8]Felici, H. M., and Drela, M., "Reduction of Numerical Diffusion in Three-Dimensional Vortical Flows Using a Coupled Eulerian/Lagrangian Solution Procedure," AIAA Paper 93-2928, July 1993.

[9]Felici, H. M., "A Coupled Eulerian/Lagrangian Method for the Solution of Three-Dimensional Vortical Flows," Ph.D. Thesis, Dept. of Aeronautics & Astronautics, Massachusetts Inst. of Technology, Cambridge, MA, June 1992.

[10]Drela, M., and Murman, E. M., "Prospects for Eulerian CFD Analysis of Helicopter Vortex Flows," American Helicopter Society Specialist Meeting, Arlington TX, Feb. 1987; also CFDL TR-87-3, Computational Fluid Dynamics Lab., Dept. of Aeronautics and Astronautics, Massachusetts Inst. of Technology, Cambridge, MA, 1987.

[11]Chorin, A. J., "A Numerical Method for Solving Incompressible Viscous Flow Problems," *Journal of Computational Physics*, Vol. 2, 1967, pp. 12–26.

[12]Felici, H. M., and Drela, M., "Eulerian/Lagrangian Solution of 3-D Rotational Flows," AIAA Paper 90-1631, June 1990.

[13]Ashley, H., and Landahl, M., *Aerodynamics of Wings and Bodies*, Addison-Wesley, Reading, MA, 1965.

[14]Hawthorne, W. R., "Secondary Circulation in Fluid Flow," *Proceedings of the Royal Society of London*, Vol. 206, 1951, p. 374.

[15]Enayet, M. M., Gibson, M. M., Taylor, A. M. K. P., and Yianneskis, M., "Laser Doppler Measurements of Laminar and Turbulent Flow in a Pipe Bend," NASA CR-3551, May 1982.

[16]Knio, O. M., and Ghoniem, A. F., "Three Dimensional Vortex Simulation of Entrainement Augmentation Due to Streamwise Structures," AIAA Paper 89-0574, Jan. 1989.